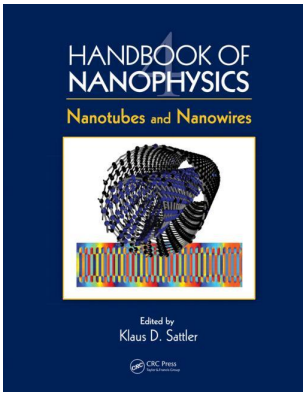

Handbook of Nanophysics
Nanotubes and Nanowires

Klaus D. Sattler

Electron Transport in Carbon Nanotubes

Publication details
https://www.routledgehandbooks.com/doi/10.1201/9781420075434-5
Na Young Kim
Published online on: 17 Sep 2010

3

Electron Transport in Carbon Nanotubes

Na Young Kim
Stanford University

3.1 Introduction

Carbon ($_6$C) exists ubiquitously in nature. It is the fourth most abundant element by mass after hydrogen, helium, and oxygen. Carbon has four valence electrons in 2*s* and 2*p* orbitals that can form three hybridization arrangements: *sp*, sp^2, and sp^3. Via these hybrid orbitals, carbon can bond to themselves and to other elements. Even with the carbon element only, there are many systems with distinct properties: diamond, graphene, and buckyball fullerene C_{60} (Figure 3.1c). It is mysterious that carbon bonding in diamond can be as strong as to scribe other crystals, but in graphite as weak as to scribble on paper.

In 1991, graphitic needle-like carbon structures were synthesized fortuitously in a furnace that was used to produce C_{60} and other fullerene structures (Figure 3.1d, Iijima 1991). Since such concentric cylindrical structures were unprecedented, in early literature they were denoted as "microtubules" (Iijima 1991), "fullerene tubules" (Mintmire et al. 1992), or "graphene tubules" (Saito et al. 1992), before the term carbon nanotube (CNT) was coined. These early terms reflected the different perspectives of newly discovered structures. One school of thought believed that CNTs could be elongated from fullerene as mutations, while another school of thought believed that they could be formed by folding several graphene layers seamlessly. Although the starting material to make needle-like carbon structures from these two thoughts was not the same, both perspectives commonly envisioned CNTs as one-dimensional (1D) objects. A high geometric ratio of length to diameter (10^5–10^6) indeed supports this 1D picture from experimental statistical analyses that diameters are typically up to a few tens of nanometers and lengths are in microns and even in millimeters.

One-dimensional systems are very special in comparison to their two-dimensional or three-dimensional counterparts in that there is only one particular direction along which particles can move freely while they are strongly confined along two other directions. Hence, scientists and engineers have longed for a physical medium to explore unique 1D properties and have searched for alternative structures to attain miniaturization. Shortly after their discovery, CNTs have been one of the hot research topics in investigating low-dimensional properties in a variety of disciplines in science and engineering.

Many researchers have been intrigued by the CNTs' extraordinary mechanical, chemical, optical, and electrical properties and their fabrication advantages (low cost and defect-free crystalline structure) (Saito et al. 1998, Harris 1999, Jorio et al. 2008). Indeed, CNTs have already been influential in widespread areas as sensitive chemical sensors, high-resolution imaging probes, field emission displays, supercapacitors, conductive flexible electrodes, and more. In particular, CNTs have been regarded as potentially promising for future molecular electronics based on their phenomenal electrical characteristics and naturally small sizes (Dekker 1999). For example, high-performance nanotube field effect transistors have been demonstrated with semiconducting tubes (Bockrath et al. 1997, Javey et al. 2003), and the interplay of electrons and phonons in CNT transistors was thoroughly examined in order to develop practical room-temperature electronics (Yao et al. 2000, Javey et al. 2004, Park et al. 2004). Due to the spatial confinement in 1D where electrons can move only back and forth in principle, several questions naturally arise: How do electrons carry electrical information in 1D conductors like CNTs? What are the unique electrical phenomena occurring in 1D conductors?

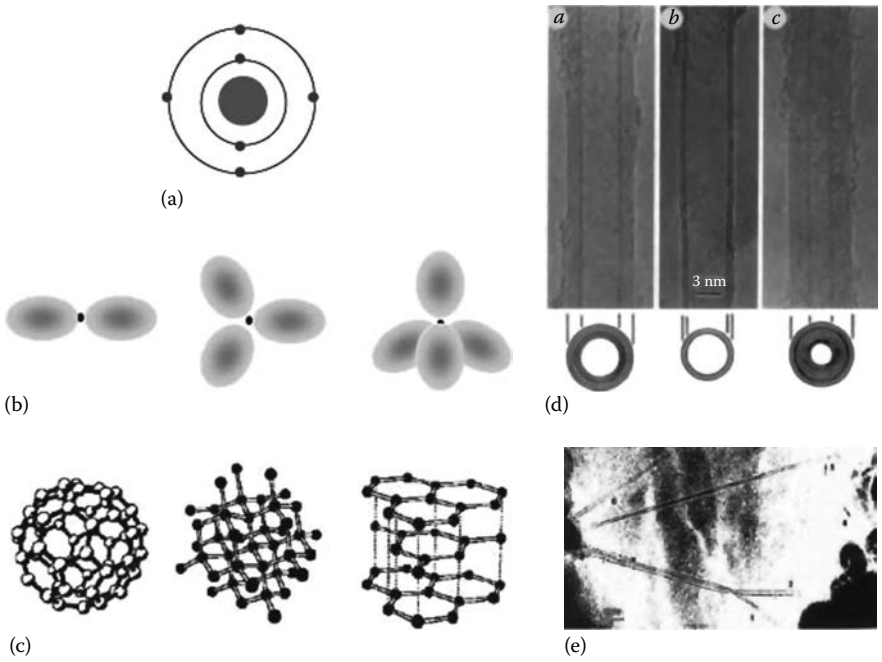

FIGURE 3.1 (a) A cartoon of the $_6$C atomic shell structure in a semiclassical picture. (b) The diagram of *s*- and *p*-orbital hybridization: linear *sp* (left), planer sp^2 (middle), and tetrahedral sp^3 (right). (c) Structures of carbon-based material: C_{60} (left), diamond (middle), and graphite (right). (d) Electron micrograph of multi-walled carbon nanotubes. (Reprinted from Iijima, S., *Nature*, 354, 56, 1991. With permission.) (e) An electron micrograph of single-walled carbon nanotubes. (Reprinted from Iijima, S. and Ichihashi, T., *Nature*, 363, 603, 1993. With permission.)

This chapter describes the fundamental concepts and recent progress in CNT electron transport fields. Electron transport measurements are convenient methods for characterizing materials in order to study the underlying physical principles. By applying external stimulations, the corresponding response of materials provides an answer to the question of how electrons flow through them. Section 3.2 provides an overview of CNT electron transport research areas and presents several basic concepts and terminologies of quantum electron transport and two theoretical frameworks pertinent for interpreting CNT transport properties. Based on these fundamentals, Section 3.3 develops the details of quantum electron transport measurements using metallic single-walled carbon nanotubes in terms of differential conductance and shot noise. A summary of the discussion and future perspectives are given in Sections 3.4 and 3.5, respectively.

3.2 Fundamental Concepts

3.2.1 Overview of Carbon Nanotube Transport

CNTs are regarded as one of the ideal 1D systems and a good candidate for exploring low dimensional physics. The basic electronic understanding of CNTs starts from their band structure. Shortly after the discovery of concentric multi-layered carbon tubules in 1991, condensed matter theorists immediately established the theoretical framework to compute the band structure of CNTs by extending the two-dimensional graphene knowledge. They first simplified a target system as one single tube that was conceptually folded from one graphene layer even before such tubes were physically identified (Mintmire et al. 1992, Saito et al. 1992).

Figure 3.2 depicts how to form CNTs from a sheet of graphene by rolling up along a certain direction with a different diameter. A (*n*, *m*) configuration classifies possible nanotubes in terms of the integer coefficients of the two-dimensional roll-up vector ($\vec{C}_h$, Figure 3.2b, Saito et al. 1992). This (*n*, *m*) configuration is a compact representation to specify diameters and chiralities of CNTs. A spatial confinement along the circumferential direction in CNTs requires satisfying a periodic boundary condition. Thus, by including this additional boundary condition into the well-established graphite band structure calculation (Wallace 1947), the CNT band structure was readily computed (Mintmire et al. 1992, Saito et al. 1992).

Condensed matter theorists conjectured from the band structure calculation that such tubules would exhibit either metallic or semiconducting behavior depending on the values of *n*, *m* (Mintmire et al. 1992, Saito et al. 1992). When *n*-*m* is an integer in multiples of 3, the (*n*, *m*) nanotubes will be metallic. Specific terms became available according to theoretical insights: single-walled nanotubes (SWNTs) and multi-walled nanotubes (MWNTs) are distinguished by the number of constituent layers; armchair ($n = m$) and zigzag tubes ($n = 0$ or $m = 0$) indicate a hexagonal arrangement around the circumference.

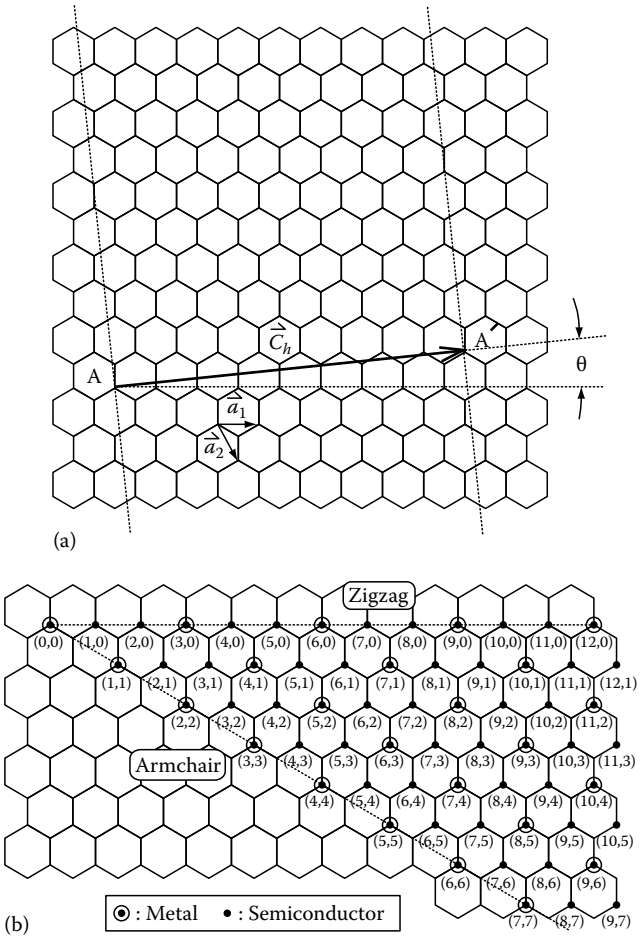

FIGURE 3.2 (a) Theoretical visualization to form a nanotube by rolling up from A to A' in a two-dimensional graphene sheet with a roll-up vector $\vec{C}_h = n\vec{a}_1 + m\vec{a}_2 \equiv (n,m)$ where $\vec{a}_1$ and $\vec{a}_2$ are two unit vectors. (b) Possible (n, m) configuration of SWNTs with various diameters with the denotation of metallic ($|n-m| = 3l$, where l is an integer) and semiconducting properties. (Reprinted from Saito, R. et al., *Appl. Phys. Lett.*, 60, 2204, 1992. With permission.)

Furthermore, these theoretical conjectures were initiated to search for SWNTs and to investigate mysterious properties. In the year 1993, another landmark in the history of the CNT research field emerged—the discovery of theoretically imagined SWNTs (Iijima and Ichihashi 1993). Finally, physical systems are now available to verify the theoretical predictions.

Early experiments using CNTs were rather limited in material investigations such as synthesis (Iijima 1991, Ebbesen and Ajayan 1992, Iijima et al. 1992, Iijima and Ichihashi 1993), chemical treatments for purifications (Ebbesen et al. 1994, Tsang et al. 1994, Tohji et al. 1996), surface imaging by scanning electron microscopy (Iijima 1991, Iijima and Ichihashi 1993), atomic force microscopy (Figure 3.3), and scanning tunneling microscopy (Ge and Sattler 1993, Wilder et al. 1998). The aforementioned experimental works confirmed unequivocally the theoretical predictions based on the band structure calculation

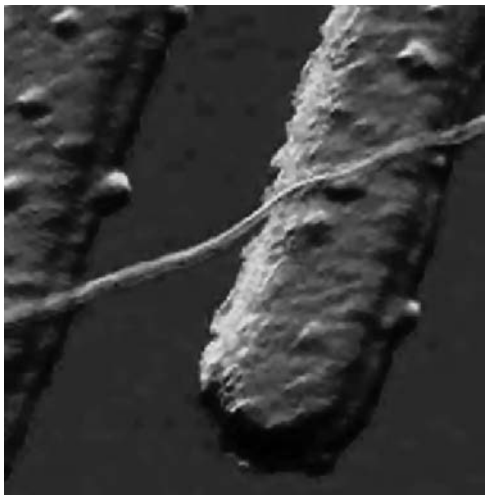

FIGURE 3.3 Atomic force microscope image of a SWNT between Pt electrodes spaced by 50 nm. (Reprinted from Tans, S.J. et al., *Nature*, 386, 474, 1997. With permission.)

of CNTs. However, in order to perform electrical transport measurements, it was critical to access individual nanotubes and to apply voltages to them. Ebbessen et al. (1996) and Tans et al. (1997) accomplished this goal and reported their first electrical access to individual SWNTs in the late 1990s.

To enhance experimental efficiency and reproducibility in electrical transport measurements, two primary issues needed to be solved. One was to synthesize nanotubes at designated locations and the other was to improve the coupling between the tube and the electrodes. The first target was achieved by using a chemical vapor deposition technique to produce high-yield, high-quality SWNTs nearby catalyst islands (Kong et al. 1998). The second target has been continuously attempted by using different metal electrodes and annealing, and recently ohmic contacted nanotube devices were fabricated (Kong et al. 2001, Liang et al. 2001, Javey et al. 2003). In addition, when integrated nanotube circuits were achieved in Si-substrates (Soh et al. 1999), the CNT transport field made rapid progress and demonstrated numerous functional devices including transistors, oscillators, and sensors by utilizing advanced semiconductor fabrication techniques.

Originating from phase-coherent electrons and strong interactions among electrons in 1D structures, quantum transport phenomena have also been continuously revealed in SWNTs coupled with electron reservoirs: Coulomb blockade (Bockrath et al. 1997, Tans et al. 1998, Postma et al. 2001), Tomonaga–Luttinger liquid behavior (Bockrath et al. 1999, Yao et al. 1999), quantum ballistic interference (Kong et al. 2001, Liang et al. 2001), Kondo (Liang et al. 2002, Nygard et al. 2000) and orbital Kondo phenomena (Jarillo-Herrero et al. 2005), Aharonov-Bohm interference (Cao et al. 2004), magnetic orbital moment determination (Minot et al. 2004), and supercurrent behavior (Jarillo-Herrero et al. 2006). Some basic concepts of quantum electron transport are introduced in the following subsection.

3.2.2 Electron Transport

Mesoscopic systems refer to materials whose physical dimensions typically span from millimeters to nanometers. A SWNT is a representative mesoscopic system. Rigorously, a SWNT is an ideal 1D system since its Fermi wavelength λ_F is shorter than a longitudinal SWNT length, L. λ_F is a wavelength of carriers at Fermi energy (E_F) level about 0.8 nm, and it is an important quantity since the majority of carriers are electrons near E_F. In such low-dimensional systems, subtle and sophisticated features appear that are deeply rooted in quantum mechanics and tightly associated with many-body interactions.

Discerned from their classical counterpart, quantum transport properties reflect unique traits of coherence and quantization in the system. Quantum transport is classified into several regimes primarily by relevant lengthscale comparison. These transport divisions are crucial in understanding transport properties in each regime. Besides λ_F, other relevant characteristic lengths are defined for classified transport regimes: (1) mean free path, l_{mfp}, (2) thermal diffusion length, l_T, and (3) phase coherence length, l_ϕ.

3.2.2.1 Mean Free Path l_{mfp}

The mean free path, as the name indicates, is the average distance in which particles can move freely. Major sources to inhibit free motions of electrons are scatterers such as defects, impurities, or grain boundaries. Elastic scattering does not conserve momentum but energy, while inelastic scattering changes both momentum and energy of incident particles. Thus, mean free paths due to elastic and inelastic scattering should be differentiated accordingly, although generally, l_{mfp} refers to the elastic mean free path. In semiconductors, l_{mfp} is closely related to the mobility of carriers, and in metals l_{mfp} is much longer than λ_F. As l_{mfp} becomes comparable to λ_F, systems with such l_{mfp} are called in the dirty limit.

3.2.2.2 Thermal Diffusion Length l_T

At nonzero temperatures, electron wavepackets have an energy width of about k_BT where k_B is the Boltzmann's constant and T is the temperature. This energy uncertainty induces diffusion in time. l_T is a characteristic length of diffusion process due to thermal energy.

3.2.2.3 Phase Coherence Length l_ϕ

Within l_ϕ, particles preserve their phase. Dynamical interactions including mutual Coulomb interactions among electrons and electron-phonon interactions disturb phase coherence. Therefore, this length is important to determine whether quantum interference effects from phase coherent sources can be detectable or not in systems.

Comparisons of such scales define three distinct transport regimes summarized in Table 3.1. Varying the physical length of mesoscopic conductors, all enlisted transport regimes are indeed within practical reach. Both in dissipative and in diffusive regimes, scattering processes determine transport quantities similar to the classical case. Elaborately, electrons in dissipative conductors suffer from inelastic as well as elastic scattering, losing the history of momentum and energy trajectories. Electrons in diffusive conductors encounter elastic scatterers so that they preserve energy but not momentum information. In the ballistic regime, on the other hand, all dimensions of ballistic conductors are much smaller than all aforementioned length scales; therefore, electrons participating in the conduction process do not encounter any kind of scattering sources, consequently, both momentum and energy are conserved in this ballistic regime.

TABLE 3.1 Classified Quantum Electron Transport Regimes. L_i ($i = x, y, z$) Represent a System Length along Each Direction

Regime	Condition
Ballistic	$L_x, L_y, L_z < l_{mpf}, l_T, l_\phi$
Diffusive	$l_{mpf}, l_T \ll L_x, L_y, L_z$
Dissipative	$l_\phi < L_x, L_y, L_z$

In principle, ballistic conductors have zero resistance, which is caused by scattering processes; however, when we measure their two-terminal resistance, it is not zero. The finite resistance occurs at the interface of a ballistic mesoscopic conductor and two metal electrodes, which are unavoidable to access the conductor (Datta 1995). This resistance does not come from scattering processes; instead it comes from the fact that the number of electron modes has to be matched between an electrode and a conductor. Metal electrodes can support infinite numbers of electron modes, whereas a mesoscopic conductor can only allow several discrete electron modes determined by spatial confinement. Hence, most of the electron modes are reflected at the interface of the metal electrode and the conductor and only a few modes are able to flow through the conductor. The reflection of electron modes yields such finite resistance. There needs to be an alternative way to express such resistance beyond Ohm's law. Landauer captured the significance of the wave nature of charge carriers in mesoscopic conductors, and he developed a theory to estimate resistance or conductance in terms of transmission probabilities of propagating electron modes analogous to electromagnetic photon modes. This "Landauer–Büttiker formalism" is one of fundamental theory to express a system conductance in terms of its quantum mechanical transmission probabilities.

3.2.2.4 Landauer–Büttiker Formalism

Suppose a simple 1D ballistic conductor coupled with bulk (3D) electron reservoirs. An adiabatic transition from bulk reservoirs to the device and zero temperature is assumed. Due to the spatial confinement, the allowed modes in the conductor are discretized whereas the modes in the bulk are relatively dense. Therefore, not all modes below the Fermi energy can propagate into the conductor due to energy and momentum conservation, yielding that only certain modes can exist in both regions. Mode

reflection at the interface of two dissimilar materials causes finite conductance even with a ballistic conductor. Sometimes this finite resistance is called "contact resistance." In the simplest case, only one channel in the conductor exists. The current I across the conductor with the applied bias voltage V is derived by definition from $I = \int_{E_F}^{E_F+eV} e\rho(E)v_g(E)\mathrm{d}E$ with energy-dependent density of states ρ, group velocity v_g, and Fermi energy E_F. The density of states ρ in 1D is written as $\rho = \frac{1}{2\pi\hbar v_g(E)}$. Note that in 1D, there is a magic cancellation of the velocity component, yielding the product of ρ and v_g is constant $1/h$. Hence, the current including spin degeneracy (a factor of 2) is

$$I = \int_{E_F}^{E_F+eV} e\frac{2}{h}\mathrm{d}E = 2\frac{e^2}{h}V \equiv G_Q V$$

where G_Q is denoted as a spin-degenerate quantum unit of conductance when the mode is completely transmitting. If partial transmission occurs with a probability τ, the conductance becomes $G_Q\tau$. Straightforwardly, this scheme can be extended to multi-mode channels whose individual transmission probability is τ_i, where the conductance G is summed over all modes, $G = G_Q\sum_i \tau_i$, known as the "Landauer formula" (Datta 1995, Imry and Landauer 1999). Since the hexagonal Brillouin zone of SWNTs contains two inequivalent K and K' points, four bands degenerate at the same energy reflecting the orbital and spin degeneracy. Therefore, the ideal resistance of SWNTs is $2G_Q = 4e^2/h \sim (6.45\,\mathrm{k\Omega})^{-1}$.

Besides conductance, noise (current fluctuations) has also been actively studied in mesoscopic conductors (Blanter and Büttiker 2000). There are several sources to generate current fluctuations that are pronounced in mesoscopic conductors: internal microscopic random processes caused by thermal fluctuations, scattering and tunneling, and quantum effects (Buckingham 1983, Blanter and Büttiker 2000). Noise theories have been developed intensively since its properties disclose correlations of charge carriers, scattering mechanisms, and quantum coherence, which are essential for understanding the electron transport properties especially in low-dimensional conductors. Recent endeavors in this direction are put into gaining a complete statistical analysis of charge transport under the name of "full counting statistics" (Levitov and Lesovik 1993, Levitov et al. 1996, Kindermann and Nazarov 2002, Nazarov et al. 2002). In the stochastic transport of quantized charged carriers, nonequilibrium current fluctuations are denoted as shot noise, the second moment of characteristic functions in the full counting statistics. What stimulates the advent of full counting statistics is the fact that higher moments provide additional information of systems beyond the first moment, conductance. The focus of this chapter lies on two moments: conductance (the first moment) and shot noise (the second moment) from which SWNTs' electronic properties are quantified.

3.2.3 Fermi-Liquid vs. Non-Fermi-Liquid Theories

Often, a single-particle picture describes macroscopic conductors and their properties sufficiently well with a valid justification of effective screening. However, in lower dimensional systems as devices shrink down, screening among particles becomes insufficient. Consequently, the many-body picture assumes a significant role. In this section, two theoretical models are introduced: the Fermi-liquid (FL) theory and the Tomonaga–Luttinger liquid (TLL) theory. The former explains nominal features within a single particle picture, whereas the latter explains the unique behaviors arising from many-body interactions particularly in 1D conductors.

3.2.3.1 Fermi-Liquid Theory

The FL theory is one of the successful solid-state frameworks to describe the physical properties of weakly interacting many-body condensed matter systems, such as the liquid state of ^{3}He and conductivity in metals and semiconductors (Mahan 2007). In the FL system, there are still non-negligible interactions among particles. However, Landau ingeniously approached the FL system with a hypothesis that interactions are adiabatically switched on. Furthermore, he considered the long wavelength limit, namely, low energy excitations near the Fermi energy. He captured the idea that the interactions would modify the energy dispersion relation, consequently changing the mass of electrons in the system. By introducing the effective mass m^*, which manifests the strength of mutual interactions, Landau established the FL theory within the single particle picture.

The essence of the FL theory is the existence of quasi-particles with the effective mass. Quasi-particles are low-lying elementary excitations consisting of electrons whose density fluctuations arise from the particle interactions. Due to the fact that quasi-particles are formed from electrons, they possess fermionic nature such as obeying Pauli Exclusion Principle. The validity of the FL theory in higher dimensions relies on effective charge screening, which reduces the long-range Coulomb interactions among electrons. Therefore, the FL theory works well to describe transport processes in systems whose interactions are short ranged and isotropic such as metals, semiconductors, and liquid ^{3}He.

3.2.3.2 Tomonaga–Luttinger Liquid Theory

The successful FL theory fails in 1D. The breakdown of the FL theory in 1D conductors can be understood intuitively in terms of inefficient charge screening. The long-range Coulomb interactions survive among strongly correlated electrons. In 1D, any excitation at a particular site spreads over the whole lattice similar to the domino effect. This collectiveness is unique in 1D excitations, and Landau's quasi-particles do not exist in 1D (Giamarchi 2004). A rigorous attempt to describe 1D electron gas systems is formulated as the TLL theory. Tomonaga and Luttinger came up with an exactly solvable model in 1D with insights that collective modes are bosonic in nature. By linearizing the dispersion relation near the Fermi level, low energy properties of system can be extracted (Voit 1994, Giamarchi 2004).

The Fermi surface of 1D consists of two points at $\pm k_F$, where k_F is the Fermi wavenumber. Particle-hole excitations in 1D are only possible near momentum $q = 0$ or $q = 2k_F$ near the Fermi points, whereas any q values below $2k_F$ are allowed for particle-hole excitations in higher dimensions by conserving the energy and momentum. In the limit of $q \to 0$ and low energy, the excitation spectrum is linear, resembling a phonon mode. This resemblance hints that the Hamiltonian of 1D electron gas system can be derived by boson-like phonon displacements as a rather intuitive approach. The positive (negative) slope at $k_F(-k_F)$ corresponds to right (left) moving channels. When interactions are renormalized in a system, the dimensionless quantity, the TLL parameter g, is defined as $g = \left(1 + \frac{V_0}{\pi\hbar v_F}\right)^{-\frac{1}{2}}$, where V_0 is the interaction potential. It is a measure of competition between the interaction potential energy and the kinetic energy. In the absence of V_0, g becomes 1, recovering the noninteracting Fermi gas system. On the other hand, $V_0 > \hbar v_F > 0$ for a repulsive Coulomb interaction leads to $g < 1$. The stronger the interactions V_0, the smaller the value of g. Note that g can also be greater than 1 if attractive Coulomb interactions are dominant among the particles. The TLL parameter g emerges in various 1D properties such as the fractional charge ge, the charge mode velocity v_F/g, and the power-exponents of correlation functions.

As one specific example of 1D conductors, metallic SWNTs have been predicted as the TLL system (Egger and Gogolin 1997, Kane et al. 1997). The transport properties in the tunneling regime, where tubes are isolated from metal reservoirs, exhibited the TLL features as the power-scaling conductance by means of the bias voltage and the temperatures (Bockrath et al. 1999). This nonlinear behavior certainly cannot be explained by a noninteracting single-particle picture. Recently, the spectral function from SWNT mats was obtained from angle-integrated photoemission measurements, which was claimed as the direct observation of the TLL features in SWNTs (Ishii et al. 2003). The TLL parameter g for the SWNT is $g = \left(1 + \frac{8e^2}{\pi\hbar v_F}\ln\left(\frac{R_S}{R}\right)\right)^{-\frac{1}{2}}$, where R_S is the screening length and R is the radius of the SWNT (Kane et al. 1997). The logarithmic dependence on R_S/R explains that the value of g is rather insensitive to the actual value of R_S (Kane et al. 1997), and the value falls between 0.2 and 0.3 with $v_F = 8 \times 10^7$ cm/s as $R_S/R > 4$. The search of the TLL behavior in SWNTs is actively pursued since the strongly correlated SWNTs serve as a basic ingredient of quantum electron entanglers (Bena et al. 2002, Recher and Loss 2002, Bouchiat et al. 2003, Crépieux et al. 2003).

3.3 Electron Transport in Carbon Nanotubes

3.3.1 Synthesis and Device Fabrication

3.3.1.1 Synthesis

The discovery of MWNTs seems fortuitous in a carbon arc-discharge chamber that was designed to produce fullerenes (Iijima 1991). Two years later, SWNTs were found by the same arc-discharge method except that catalytic components had been added into the chamber (Iijima and Ichihashi 1993). For a systematic characterization of new materials toward functional device fabrication and quantum nature investigation, efficient synthesis methods have been on demand that aim to isolate individual nanotubes and grow specific types of SWNTs in a controllable way. There are three major synthetic methods for growing SWNTs using catalytic nanoparticles: electric arc-discharge, laser ablation, and chemical vapor deposition (CVD). Among them, the CVD method has been superior in producing high-quality SWNTs.

Typically, the CVD chamber for growing SWNTs in the laboratory consists of a 1 in. diameter tube vessel inserted into a furnace, gas sources of CH_4, H_2 and Ar, a Si-substrate containing catalyst islands, and an exhaust system. Catalysts are essential for designating the location of SWNTs during growth. In 1999, Professor Dai's group managed to synthesize a high-yield of SWNTs near the catalyst islands. Iron-based alumina-supported catalysts were under a carbon feedstock: 99.999% CH_4 and H_2 at the right concentration for 5–7 min at 900°C–1000°C followed by an Ar flush and a cool-down to room temperature (Kong et al. 1998). This work has advanced the SWNT research field in which ballistic transport studies could be performed and prototypes of nanotube-electronics can be built.

The synthesis mechanism of SWNTs in the catalytic CVD method is associated with the details of nanoparticles. Recently, Li et al. (2001) have attempted to assess the role of catalysts and have shown that the diameter of SWNTs indeed closely links to the nanoparticle size based on statistical analysis. The report presents that the synthesis can be understood in three stages: First, nanoparticles as catalysts absorb decomposed carbon atoms from CH_4 or other carbon feedstock in the CVD process. Second, the absorption of carbon atoms to nanoparticles continues until saturation. Once it reaches the saturation point, carbon atoms start to grow outward from the catalysts with a closed-end. Third, an excess carbon supply adds to the carbon precipitation on the surface, yielding finite-length nanotubes in the end. It is reasonable, therefore, that the SWNT diameter would be determined by the nanoparticle size as the initial basis. Although Li et al. (2001) provided valuable information as to the microscopic level of understanding of the synthesis in the catalytic CVD process, the complete controllability to produce tailor-made SWNTs with an expected diameter, chirality (roll-up vector direction), length, position, and orientation on demand is yet to be acquired, which is the present SWNT fabrication challenge. Once this goal is achieved, it is not difficult to imagine that SWNTs would become widely utilized in various applications as electrical, chemical, mechanical, and optical components.

3.3.1.2 Device Fabrication

The configuration of SWNT devices for electron transport measurements resembles conventional semiconductor field-effect transistors, which have three terminals: source, drain, and gate. The fabrication goal is to produce three-terminal isolated SWNT nanotube devices on top of a Si-wafer. Figure 3.4 shows

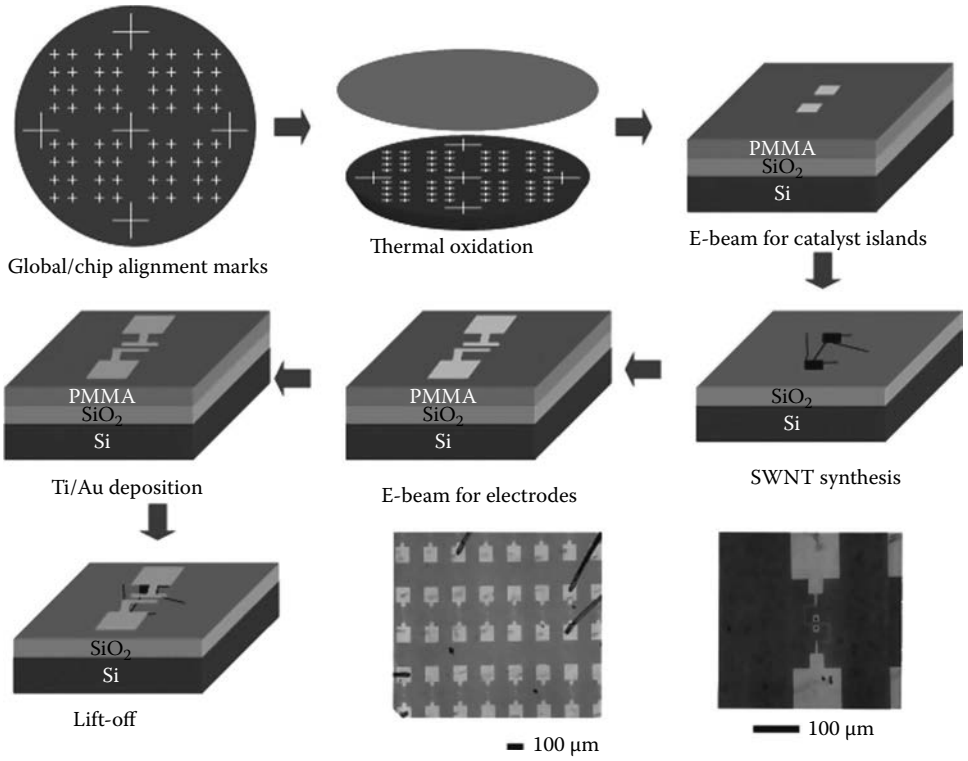

FIGURE 3.4 Schematics of the SWNT device fabrication processes. Two right bottom photographs show multiple devices in a single chip and an individual SWNT device. (From Bockrath, M. et al., *Nature*, 397, 598, 1999. With permission.)

the steps of conventional fabrication processes. Combinations of standard photolithography and electron-beam lithography (EBL) techniques enable one to produce about one hundred devices in a 1 cm × 1 cm Si substrate chip during a short period of time.

The starting material is a 4 in. heavily doped Si-wafer, which serves as a backgate to control the electron density or the Fermi energy of carbon nanotubes. First, global wafer marks and chip marks should be patterned in the blank wafer. These marks are very useful primarily in that the overlapping processes can be performed within the lithographic resolution limit and also in that they draw boundaries of chips in the whole wafer along which the wafer can be cleaved into each chip for further steps. Those alignment marks are patterned by a photolithography recipe: photoresist spin-coating followed by exposure and development, etching process, and removal of the resist. The second step is the thermal oxidation on top of the marked Si-wafer. It is a very critical step to avoid any possible impurities on wafers during this process, since any dirt on the wafers would lead to a current leakage when devices are biased. Therefore, before inserting the wafer to a diffusion furnace, the wafer should be cleaned thoroughly and properly through the diffusion wet bench process. The next task is to pattern catalyst islands at intended locations using the EBL method consisting of polymethylmethacrylate EBL resist coating, exposure, and development. Nanotubes are then synthesized by the aforementioned CVD method with methane and hydrogen gas. The second EBL is processed for patterning metal electrodes followed by thin metal deposition and a lift-off in acetone.

Once devices are prepared, at room temperature several preliminary characterizations are performed. Atomic force microscopy imaging measurements give the number of SWNTs between the electrodes and differentiate SWNTs from MWNTs based on the tube height. Nanotubes, whose diameters are 1.5–3.5 nm from atomic force microscopy (AFM) images, are presumably considered to be SWNTs according to the statistical analysis at a given recipe. AFM images cannot identify a SWNT, MWNT, or a double-walled nanotube with certainty unlike transmission electron microscopy (TEM). Since TEM requires conducting substrates, transport devices on top of Si-substrates are not quite adequate to TEM at this time. Thus, the determination of SWNTs or MWNTs relies heavily on the statistics of TEM results with synthesized nanotubes on conducting substrates by the same growth recipe.

The current (I) vs. drain-source voltage (V_{ds}) characteristics are measured by varying gate voltages (V_g). This room-temperature electrical characterization has a particular purpose to tell metallic tubes from semiconducting tubes. Metallic tubes have weak or no dependence on V_g in principle since there are always free electrons no matter where the Fermi energy lies. On the other hand, semiconducting tubes, where there is an energy gap between conduction and valence bands, exhibit strong V_g dependent I–V characteristics. When the Fermi energy lies in the energy gap regime, current values through tubes are suppressed to zero. In this way, no or very weak $-V_g$-dependent tubes can be selected,

and room-temperature characterization has also another purpose to identify the best and good ohmic contacted devices for low-temperature measurements.

The subsequent two sections describe low-temperature electron transport properties: differential conductance and low-frequency shot noise. The main discussion focuses on three-terminal metallic SWNT devices that are well contacted to electrodes. The device dimension is fixed between 200 and 600 nm by a distance between two electrodes. The Ti/Au, Ti-only, and Pd metal electrodes are used, which feature low-resistance contacts. Metallic SWNTs are considered to have both the elastic and the inelastic mean free path at least on the order of microns at low temperatures. Therefore, the electron transport within 200–600 nm-long SWNTs is believed to be ballistic, where quantum coherence is preserved inside (Kong et al. 2001, Liang et al. 2001).

3.3.2 Differential Conductance

At low temperatures, an interference pattern in differential conductance was observed in well-contacted SWNTs to Ti/Au metals with finite reflection coefficients, as shown in Figure 3.5. This diamond interference pattern arises from quantum coherence along a finite SWNT length (longitudinal confinement) due to the potential barriers at the interfaces with two metal electrodes. The spatial confinement quantizes energy levels and the energy spacing between maxima corresponds to $\Delta E = \hbar v_F/L$, where L is the SWNT length. The inset in Figure 3.5 shows that the diamond structure size is inversely proportional to L.

Liang et al. modeled this system as an electronic analog Fabry-Perot (FP) cavity as a two-channel double-barrier problem using the Landauer–Büttiker formalism within the context of the FL theory. They captured the wave nature of electrons through an isolated nanotube as an electron waveguide. Two interfaces at metal and tubes have a one-to-one correspondence with partially reflecting mirrors in the FP interferometer (Liang et al. 2001). Similar to photons in the FP cavity, electrons would experience multiple reflections between two barriers separating the metal reservoirs from the SWNT before escaping. The approach is to establish three 4×4 scattering matrices at the left and right interfaces and inside the tube. The scattering matrices contain energy-dependent components, satisfying unitary property by Born approximation (Liang et al. 2001). In metallic infinite SWNTs, forward scatterings are dominant in comparison to backscattering and interbranch scattering. Backscattering and interbranch scattering require a big momentum transfer of $2k_F$ between two K points in the Brillouin zone and satisfy the symmetry selection rules between two orthogonal π and π^* bondings among p_z-orbitals. Thus, in principle, such scattering processes inside tubes are prohibited. However, backscattering can occur at the interfaces between metal electrodes and the tube that increases the overall resistance. Meanwhile, inside the ballistic tube, the phase is accumulated over multiple reflections. The differential conductance is calculated by a simple expression,

$$\frac{dI}{dV} = \frac{2e^2}{h} \sum_{i=1}^{2} \mathrm{Tr}(S^{T^*} S),$$

taking a trace of the total scattering matrix, S. Indeed, this noninteracting theoretical model reproduces quantum interference diamond patterns within a ±10 mV bias voltage range, supporting that the observation of quantum interference is the evidence of the ballistic transport. Note that the diamond structure is persistent regardless of the bias voltage window in this FL model.

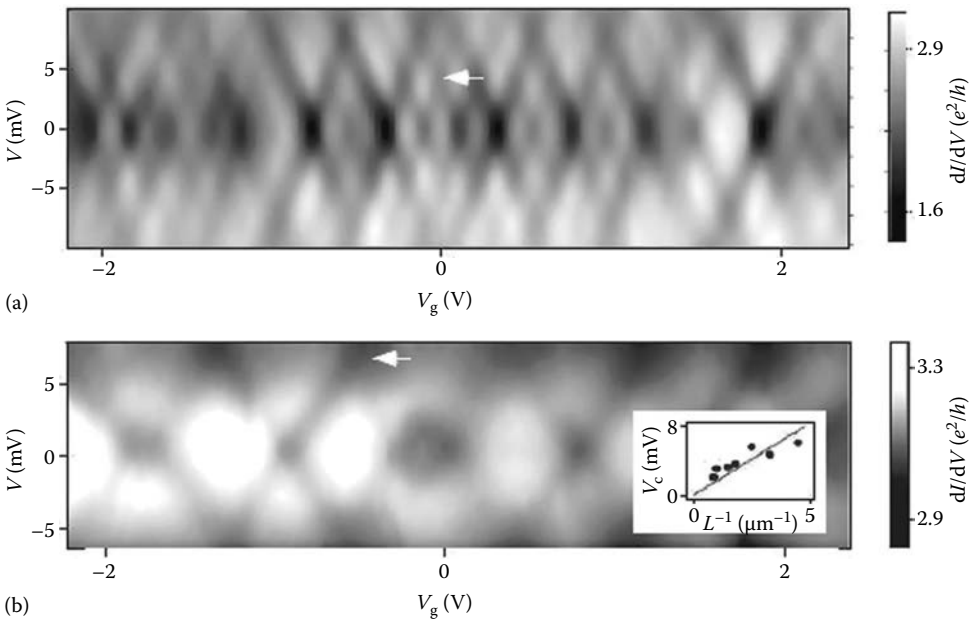

FIGURE 3.5 Two-dimensional image plot of differential conductance (dI/dV) as a function of drain-source voltage (V) and gate voltage (V_g). dI/dV is renormalized by e^2/h. There is a clear interference pattern whose feature is dependent on the SWNT length, (a) a 530 nm long SWNT device and (b) a 220 nm long SWNT device. (Reprinted from Liang, W. et al., *Nature*, 411, 665, 2001.)

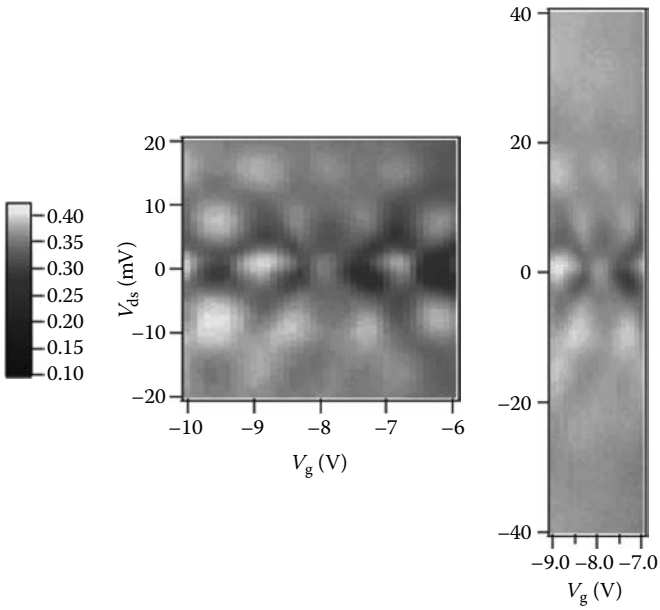

FIGURE 3.6 Density plot of differential conductance in units of $2G_Q$ against two voltages, V_{ds} and V_g. (From Liang, W., *Nature*, 411, 665, 2001. With permission.)

However, FP quantum interference pattern fringe contrast becomes reduced in magnitude at high drain-source voltages (V_{ds}). Figure 3.6 clearly exhibits that the diamond structure disappears as V_{ds} increases above 20 mV. This feature cannot be explained by the standard FL theory, which predicts constant oscillation amplitude regardless of the bias voltage values.

An alternative attempt to explain this experimental data is to model the SWNT device within the TLL theory. It is motivated by the fact that SWNTs have exhibited the features of strong correlations among charge carriers in experiments (Bockrath et al. 1999) and in theories (Egger and Gogolin 1997, Kane et al. 1997, Peça et al. 2003) owing to intrinsic many-body interactions in 1D systems. The device consisting of a ballistic SWNT and two metal electrodes is theoretically simplified as one infinite 1D conductor with two different values of the TLL parameter g for the SWNT and metal electrodes. The interaction is assumed to be strong in the SWNT ($0 < g < 1$) and weak in the higher dimensional metal reservoirs ($g = 1$) for metals (Peça et al. 2003, Recher et al. 2006). The four conducting transverse channels of the SWNTs in the FL theory are transformed to four collective excitations in the TLL theory: one interacting collective mode of the total charge and three neutral noninteracting collective modes including spin. There are two distinct propagating velocities, $v_c = v_F/g$ (the total charge mode) and v_F (the rest of three modes).

The inter-channel and intra-channel scattering processes are assumed to be allowed to reflect channels partially only at the two barriers. The application of nonzero bias voltages is treated within Keldysh formalism, a powerful method to study nonequilibrium many-body condensed-matter systems in terms of Green's functions (Mahan 2007). The transport properties are computed from correlation and retarded Green's functions (Recher et al. 2006). Three noninteracting modes encounter backscattering at the physical barrier, whereas the interacting mode encounters the momentum-conserving backscattering due to g mismatch at the interfaces in addition to the physical barrier backscattering. It was found that one interacting mode exhibits the power-law behavior, whereas three noninteracting modes still show oscillatory behavior. The overall behavior combining two effects more closely resembles the real experiments. In Figure 3.7, experimental data (left) are compared with theoretical graphs (right) at three V_g voltages (blue, green, red). Note that the tendency of amplitude reduction in experimental data cannot be reproduced by the reservoir heating model (Henny et al. 1999), which asserts that the dissipated power $V_{ds}^2(dI/dV_{ds})$ leads to a bias-voltage-dependent electron temperature (Liang et al. 2001).

Figure 3.7, furthermore, presents the following pronounced features: the period of the oscillations at low V_{ds} depends on the value of V_g, and it becomes elongated at high V_{ds}. The TLL model suggests that the elongated period appears when there is nonzero contribution to the overall oscillation by only interacting mode (propagating at a slower group velocity v_c) while those from the three noninteracting modes (propagating at Fermi velocity v_F) are completely canceled by destructive interference. This V_g-dependent oscillation period in differential conductance has been interpreted as a signature of spin-charge separation

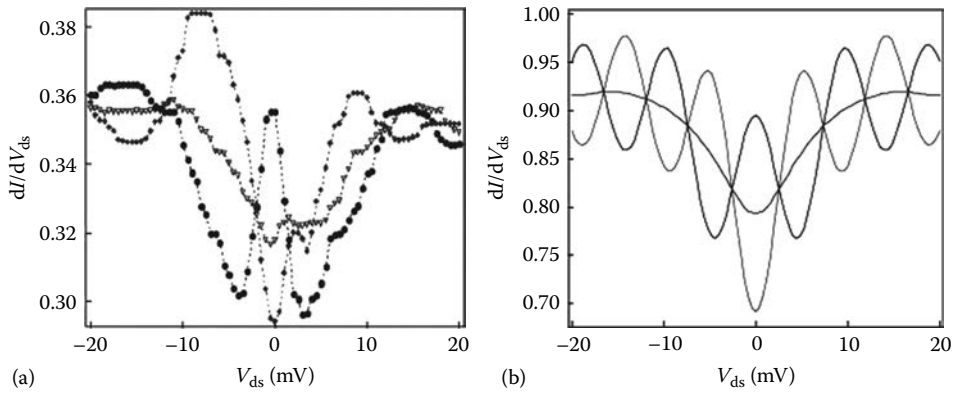

FIGURE 3.7 (a) Experimental and (b) theoretical differential conductance traces at $V_g = -9$ V (diamond in (a), line with peak at V = 0 V in (b)), −8.3 V (triangle in (a), line without oscillation in (b)), and −7.7 V (circle in (a), line with dip at V = 0 V in (b)) at 4 K.

in the SWNT (Peça et al. 2003). A comparison of the primary periods at different V_g values yields the TLL parameter $g \sim 0.22$, which is consistent with the predicted g values in SWNT. Although it seems to be compelling evidence, further experiments focusing on the periodicity with V_{ds} should be performed to be conclusive.

3.3.3 Low-Frequency Shot Noise

The low-frequency shot noise probes the second-order temporal correlation of electron current in the nonequilibrium condition. It often manifests certain microscopic physical mechanisms of the conduction process. When Poisson statistics govern the emission of electrons from a reservoir electrode, in other words, the propagation of an electron has no relationship with the previous or the successive electron, the spectral density of the current fluctuations reaches its full shot noise spectral density, $S_I = 2eI$, where I is the average current. In a mesoscopic conductor, nonequilibrium shot noise occurs due to the random partitioning of electrons by a scatterer, and it may be further modified as a consequence of the quantum statistics and interactions among charged carriers (Blanter and Büttiker 2000). A conventional measure for characterizing the shot noise level in mesoscopic conductors is the Fano factor $F \equiv S_{I,m}/2eI$, the ratio of the measured noise power spectral density $S_{I,m}$ to the full shot noise value ($2eI$). In statistics, the Fano factor is related to be a variance-to-mean ratio, so a Poisson process whose variance equals to mean yields $F = 1$. Despite growing interest in the shot noise properties of the TLLs, current noise measurements in nanotubes have only recently been executed due to the difficulty of achieving highly transparent ohmic contacts and a high signal-to-noise ratio between the weak excess-noise signal and the prevalent background noise (Roche et al. 2002), although the shot noise properties of SWNTs in the tunneling (strong barriers between metals and SWNTs) regime with the TLL features have been reported recently (Onac et al. 2006).

In the ballistic regime, the shot noise properties reveal the TLL features in the SWNT device unambiguously. Two-terminal shot noise measurements were implemented at 4 K. It is critical to calibrate an experimental apparatus to reach an accurate data acquisition and analysis. For this purpose, two current noise sources are placed in parallel: a SWNT device and a full shot noise generator. The well-characterized full shot noise source quantifies complicated cryogenic transfer functions and filters. The standard of such sources is a weakly coupled light emitting diode (LED) and photodiode (PD) pair. At 4 K, the overall coupling efficiency from the LED input current to the PD output current was about 0.1%, which eliminated completely the shot noise squeezing effect due to the constant current operation (Kim and Yamamoto 1997). In order to recover the weak shot noise of the SWNT embedded in the background thermal noise, an AC modulation lock-in technique is implemented and a resonant tank-circuit together with a home-built cryogenic low-noise preamplifier is incorporated (Reznikov et al. 1995, Liu et al. 1998, Oliver et al. 1999). The specific shot noise measurement techniques for the SWNT devices are described in detail by Kim et al. (2007).

Figure 3.8a presents a typical log–log plot (base 10) of S_{SWNT} in V_{ds} at a particular V_g. S_{SWNT} (dot) is clearly suppressed to values below full shot noise S_{PD} (triangle), and it suggests that the relevant backscattering for shot noise is indeed weak. Note that S_{SWNT} and S_{PD} have clearly different scaling slopes vs. V_{ds}. The deviation from the full shot noise in the SWNT device is beyond the scope of the FL theory. Hence, the previous TLL theory for differential conductance is extended to compute the low-frequency shot noise spectral density, $S_{SWNT} = \int dt e^{i\omega t} \left\langle \{\delta\hat{I}(t), \delta\hat{I}(0)\} \right\rangle$ with $\delta\hat{I}(t) = \hat{I}(t) - \bar{I}$, the current fluctuation operator, and the anticommutator relation $\{\delta\hat{I}(t), \delta\hat{I}(0)\} = \delta\hat{I}(t)\delta\hat{I}(0) + \delta\hat{I}(0)\delta\hat{I}(t)$ (Recher et al. 2006).

The SWNT noise in the zero-frequency limit is expressed as

$$S_{SWNT} = 2e \coth\left(eV_{ds}/2k_BT\right) I_B + 4k_BT(dI/dV_{ds} - dI_B/dV_{ds})$$

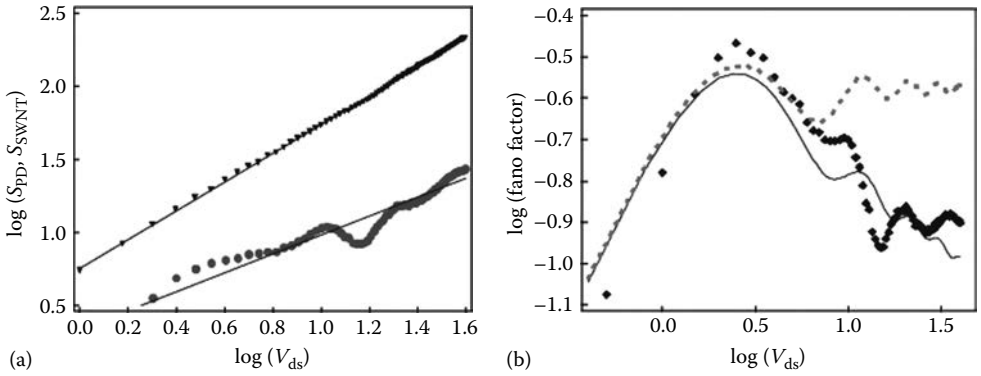

FIGURE 3.8 (a) Shot noise power spectral density vs. V_{ds} for the LED/PD pair (S_{PD}, triangle) and the SWNT (S_{SWNT}, dot) at $V_g = -7.9$ V. The slopes of S_{PD}, S_{SWNT} are 1 and 0.64, respectively. The inferred g value for the SWNT is 0.16. (b) Fano factor vs. V_{ds} on a log–log scale. The theoretical Fano factor curves where thermal noise $4k_BT(dI/dV_{ds})$ is subtracted are drawn for $g = 1$ (dotted line) and $g = 0.25$ (straight line) at $T = 4$ K. The power exponent α is −0.35 for the measured Fano factor (diamond) at $V_g = -7.9$ V., and the inferred g value is 0.18. The theoretical $g = 1$ (dotted line) plot gives $\alpha \sim 0$ as expected.

where I_B is the backscattered current. In the limit of $eV_{ds} > k_BT$, the SWNT noise spectral power density becomes simplified as $S_{SWNT} = 2eI_B$. The asymptotic behavior of I_B follows the power-law scaling $I_B \sim V_{ds}^{1+\alpha}$ with $\alpha = -(1/2)(1 - g)/(1 + g)$. The power exponent α is uniquely determined by the TLL parameter g.

The experimental Fano factor $F(V_{ds})$ is displayed on a log–log (base 10) scale in Figure 3.8b. The TLL model predicts that at low bias voltages $eV_{ds} < k_BT < \hbar/2gt_F$, experimental Fano factor F_{exp} is proportional to V_{ds} if we subtract the thermal noise component. In addition, the slope between F_{exp} and V_{ds} is insensitive to g-values in the region of $\log(V_{ds}) < \log(\hbar/2gt_F) \sim 0.47$. On the other hand, if $eV_{ds} > \hbar/2gt_F$, a power-law $F \sim V_{ds}^{\alpha}$ is expected by assumption that the backscattered current is smaller than the ideal current $2G_QV_{ds}$. A linear regression analysis of the Fano factor F with V_{ds} in this region, therefore, is another means to obtain the g value. The Fano factors F for $g = 0.25$ (red) and $g = 1$ (yellow) are displayed on a log–log scale in Figure 3.8b. The experimental data (diamonds) agree well with the theoretical Fano factor of $g = 0.25$. The stiffer slope (α) corresponds to a stronger electron–electron interaction. The measured exponent α and inferred g values from the spectral density and the Fano factor from four different devices with various metal electrodes (Ti/Au, Ti-only, Pd) show similar statistics of $\alpha \sim -0.31 \pm 0.047$ and $g \sim 0.26 \pm 0.071$ as derived from several V_g values for each sample. Many-body TLL behavior in the ballistic SWNT is clearly probed in the shot noise properties.

3.4 Summary

The electron transport properties of SWNTs are discussed based on experimental results and theoretical models. The discussion started from the discovery of carbon nanotubes and the history of their research field with a focus on the electron transport area. The noninteracting FL and interacting TLL theories, which have been used widely for bulk and 1D systems respectively, are briefly introduced as background knowledge. The ballistic transport regime is clearly defined, in which no inelastic and elastic scattering occurs, consequently quantum coherence is preserved.

A metallic SWNT is a model system to investigate ballistic transport properties in 1D owing to quantum many-body interactions. The differential conductance and the shot noise have been measured, and their experimental signatures are examined by the FL and the TLL theoretical frameworks. It is clear that quantum coherent properties manifest as an interference pattern in differential conductance, and unique power-law scaling behavior quantifies correlations among charge carriers. A noninteracting picture may describe conductance data in the low bias regime; however, it fails to explain the high-energy regions of experimental data. The TLL theory has explained the qualitative trend of conductance as a function of the drain-source voltage. In addition, it has captured the quantitative information of the strong electron–electron interactions both in conductance and the shot noise quantities. The strength of the interactions is parameterized by the TLL parameter, g, which has been obtained from the conductance period at various V_g and power-law scaling exponents from both shot noise and the Fano factor. The search of many-body collective phenomena in SWNT devices would provide fundamental physical knowledge in 1D electron transport properties.

3.5 Future Perspective

CNTs have been greatly influential in numerous areas based on extraordinary properties in physics, chemistry, chemical engineering, mechanical engineering, electrical engineering, and more. In particular, conductance and shot noise properties are important because they would ultimately provide the limiting performance of electronic devices. This chapter focuses on the early work of this property on a particular type of carbon nanotubes: metallic SWNTs. However, there has been growing interest with regard to these current fluctuations of diverse SWNT device structures. The knowledge acquired from SWNTs can certainly be transferred to other 1D systems and also carbon nanotube mother material including fullerene and graphene (Bréchignac et al. 2007, Dupas et al. 2007). At present, an experimental investigation on graphene is indeed very exciting and progressively moving forward in comparison with carbon nanotube properties. Therefore, this field will continue to deepen low-dimensional physical knowledge and to build pragmatic devices and systems that can impact everyday lives of human beings (Baughman et al. 2002).

References

Baughman, R. H., Zakhidov, A. A., and de Heer, W. A. 2002. Carbon nanotubes—The route toward applications. *Science* 297: 787–792.

Bena, C., Vishveshware, S., Balents, L., and Fisher, M. P. A. 2002. Quantum entanglement in carbon nanotubes. *Phys. Rev. Lett*. 89: 037901.

Blanter, Ya. M. and Büttiker, M. 2000. Shot noise in mesoscopic conductors. *Phys. Rep*. 336: 1–166.

Bockrath, M., Cobden, D. H., McEuen, P. L. et al. 1997. Single-electron transport in ropes of carbon nanotubes. *Science* 275: 1922–1925.

Bockrath, M., Cobden, D. H., Lu, J. et al. 1999. Luttinger-liquid behavior in carbon nanotubes. *Nature* 397: 598–601.

Bouchiat, V., Chtchelkatchev, N., Feinberg, D., Lesovik, G. B., Martin, T., and Torres, J. 2003. Single-walled carbon nanotube-superconductor entangler: Noise correlations and Einstein-Podolsky-Rosen states. *Nanotechnology* 14: 77–85.

Bréchignac, C., Houdy, P., and Lahmani, M. 2007. *Nanomaterials and Nanochemistry*. Berlin/Heidelberg, Germany: Springer.

Buckingham, M. J. 1983. *Noise in Electronic Devices and Systems*. New York: John Wiley & Sons.

Cao, J., Wang, Q., Rolandi, M., and Dai, H. 2004. Aharonov-Bohm interference and beating in single-walled carbon-nanotube interferometers. *Phys. Rev. Lett*. 93: 216803.

Crépieux, A., Guyon, R., Devillard, P., and Martin, T. 2003. Electron injection in a nanotube: Noise correlations and entanglement. *Phys. Rev. B* 67: 205408.

Datta, S. 1995. *Electronic Transport in Mesoscopic Systems*. Cambridge, U.K.: Cambridge University Press.

Dekker, C. 1999. Carbon nanotubes as molecular quantum wires. *Phys. Today* 5: 22–28.

Dupas, C., Houdy, P., and Lahmani, M. 2007. *Nanoscience—Nanotechnologies and Nanophysics*. Berlin/Heidelberg, Germany: Springer.

Ebbesen, T. W. and Ajayan, P. M. 1992. Large-scale synthesis of carbon nanotubes. *Nature* 358: 220–222.

Ebbesen, T. W., Ajayan, P. M., Hiura, H., and Tanigaki, K. 1994. Purification of nanotubes. *Nature* 367: 519.

Ebbesen, T. W., Lezec, T. H., Hiura, H., Bennett, J. W., Ghaemi, H. F., and Thio, T. 1996. Electrical conductivity of individual carbon nanotubes. *Nature* 382: 54–56.

Egger, R. and Gogolin, A. O. 1997. Effective low-energy theory for correlated carbon nanotubes. *Phys. Rev. Lett*. 79: 5082–5085.

Ge, M. and Sattler, K. 1993. Vapor-condensation generation and {STM} analysis of fullerene tubes. *Science* 260: 515–518.

Giamarchi, T. 2004. *Quantum Physics in One Dimension*. Oxford, U.K.: Oxford University Press.

Harris, P. J. F. 1999. *Carbon Nanotubes and Related Structures: New Materials for the Twenty-First Century*. Cambridge, U.K.: Cambridge University Press.

Henny, M., Oberholzer, S., Strunk, C., and Schonenberger, C. 1999. 1/3-Shot-noise suppression in diffusive nanowires. *Phys. Rev. B* 59: 2871–2880.

Iijima, S. 1991. Helical microtubules of graphitic carbon. *Nature* 354: 56–58.

Iijima, S. and Ichihashi, T. 1993. Single-shell carbon nanotubes of 1-nm diameter. *Nature* 363: 603–605.

Iijima, S., Ichihashi, T., and Ando, Y. 1992. Pentagons, heptagons and negative curvature in graphite microtubule growth. *Nature* 356: 776–778.

Imry, Y. and Landauer, R. 1999. Conductance viewed as transmission. *Rev. Mod. Phys*. 71: S306–S312.

Ishii, H., Kataura, H., Shiozawa, H. et al. 2003. Direct observation of Tomonaga-Luttinger-liquid state in carbon nanotubes at low temperatures. *Nature* 426: 540–544.

Jarillo-Herrero, P., Kong, J., Van der Zant, H. S. J. et al. 2005. Orbital Kondo effect in carbon nanotubes. *Nature* 434: 484–488.

Jarillo-Herrero, P., van Dam, J., and Kouwenhoven, L. 2006. Quantum supercurrent transistors in carbon nanotubes. *Nature* 439: 953–956.

Javey, A., Guo, J., Paulsson, M. et al. 2004. High-field quasi ballistic transport in short carbon nanotubes. *Phys. Rev. Lett*. 92: 106804.

Javey, A., Guo, J., Wang, Q., Lundstrom, M., and Dai, H. 2003. Ballistic carbon nanotube field-effect transistors. *Nature* 424: 654–657.

Jorio, A., Dresselhaus, G., and Dresselhaus, M. S. 2008. *Carbon Nanotubes: Advanced Topics in the Synthesis, Structure, Properties and Applications*. Berlin/Heidelberg, Germany: Springer.

Kane, C., Balents, L., and Fisher, M. P. A. 1997. Coulomb interactions and mesoscopic effects in carbon nanotubes. *Phys. Rev. Lett*. 79: 5086–5089.

Kim, J. and Yamamoto, Y. 1997. Theory of noise in P-N junction light emitters. *Phys. Rev. B* 55: 9949–9959.

Kim, N. Y., Recher, P., Oliver, W. D., Yamamoto, Y., Kong, J., and Dai, H. 2007. Tomonaga-Luttinger liquid features in ballistic single-walled carbon nanotubes: Conductance and shot noise. *Phys. Rev. Lett*. 99: 036802.

Kindermann, M. and Nazarov, Yu. V. 2002 Full counting statistics in electric circuits. In *Quantum Noise in Mesoscopic Physics*, eds. Yu. V. Nazarov and Ya. M. Blanter, pp. 403–429. Dordrecht, the Netherlands: Kluwer Academic Publishers.

Kong, J., Soh, H. T., Cassell, A. M., Quate, C. F., and Dai, H. 1998. Synthesis of individual single-walled carbon nanotubes on patterned silicon wafers. *Nature* 395: 878–881.

Kong, J., Yenilmez, E., Tombler, T. W. et al. 2001. Quantum interference and ballistic transmission in nanotube electron waveguides. *Phys. Rev. Lett*. 87: 106801.

Levitov, L. S., Lee, H., and Lesovik, G. B. 1996. Electron counting statistics and coherent states of electric current. *J. Math. Phys*. 37: 4845–4866.

Levitov, L. S. and Lesovik, G. B. 1993. Charge distribution in quantum shot noise. *JETP Lett*. 58: 230–235.

Li, Y., Kim, W., Zhang, Y., Rolandi, M., Wang, D., and Dai, H. 2001. Growth of single-walled carbon nanotubes from discrete catalytic nanoparticles of various sizes. *J. Phys. Chem. B* 105: 11424–11431.

Liang, W., Bockrath, M., Bozovic, D., Hafner, J. H., Tinkham, M., and Park, H. 2001. Fabry-Perot interference in a nanotube electron waveguide. *Nature* 411: 665–669.

Liang, W., Bockrath, M., and Park, H. 2002. Shell filling and exchange coupling in metallic single-walled carbon nanotubes. *Phys. Rev. Lett*. 88: 126801.

Liu, R. C., Odom, B., Yamamoto, Y., and Tarucha, S. 1998. Quantum interference in electron collision. *Nature* 391: 263–265.

Mahan, G. D. 2007. *Many-Particle Physics*. New York: Springer.

Minot, E. D., Yaish, Y., Sazonova, V., and McEuen, P. L. 2004. Determination of electron orbital magnetic moments in carbon nanotubes. *Nature* 428: 536–539.

Mintmire, J. W., Dunlap, B. I., and White, C. T. 1992. Are fullerene tubules metallic? *Phys. Rev. Lett*. 68: 631–634.

Nazarov, Yu. V. and Bagrets, D. A. 2002. Circuit theory for full counting statistics in multiterminal circuits. *Phys. Rev. Lett*. 88: 196801.

Nygard, J., Cobden, D. H., and Lindelof, P. E. 2000. Kondo physics in carbon nanotubes. *Nature* 408: 342–346.

Oliver, W. D., Kim, J., Liu, R. C., and Yamamoto, Y. 1999. Hanbury Brown and Twiss-type experiment with electrons. *Science* 284: 299–302.

Onac, E., Balestro, F., Trauzettel, B., Lodewijk, C. F. J., and Kouwenhoven, L. P. 2006. Shot-noise detection in a carbon nanotube quantum dot. *Phys. Rev. Lett*. 96: 026803.

Park, J., Rosenblatt, S., Yaish, Y. et al. 2004. Electron-phonon scattering in metallic single-walled carbon nanotubes. *Nano Lett*. 4: 517–520.

Peça, C. S., Balents, L., and Wiese, K. J. 2003. Fabry-Perot interference and spin filtering in carbon nanotubes. *Phys. Rev. B* 68: 205423.

Postma, H. W. Ch., Teepen, T, Yao, Z., Grifoni, M., and Dekker, C. 2001. Carbon nanotube single-electron transistors at room temperature. *Science* 293: 76–79.

Recher, P., Kim, N. Y., and Yamamoto, Y. 2006. Tomonaga-Luttinger liquid correlations and Fabry-Perot interference in conductance and finite-frequency shot noise in a single-walled carbon nanotube. *Phys. Rev. B* 74: 235438.

Recher, P. and Loss, D. 2002. Superconductor coupled to two Luttinger liquids as an Entangler for electron spins. *Phys. Rev. B* 65: 165327.

Roche, P.-E., Kociak, M., Gueron, S., Kasumov, A., Reulet, B., and Bouchiart, H. 2002. Very low shot noise in carbon nanotubes. *Euro. Phys. J. B* 28: 217–222.

Reznikov, M., Heiblum, H., Shtrikman, H., and Mahalu, D. 1995. Temporal correlation of electrons: Suppression of shot noise in a ballistic quantum point contact. *Phys. Rev. Lett*. 75: 3340–3343.

Saito, R., Dresselhaus, G., and Dresselhaus, M. S. 1998. *Physical Properties of Carbon Nanotubes*. London, U.K.: Imperial College Press.

Saito, R., Fujita, M., Dresselhaus, G., and Dresselhaus, M. S. 1992. Electronic structure of chiral graphene tubules. *Appl. Phys. Lett*. 60: 2204–2206.

Soh, H. T., Quate, C. F., Morpurgo, A. F., Marcus, C. M., Kong, J., and Dai, H. 1999. Integrated nanotube circuits: Controlled growth and ohmic contacting of single-walled carbon nanotubes. *Appl. Phys. Lett*. 75: 627–629.

Tans, S. J., Devoret, M. H., Dai, H. et al. 1997. Individual single-wall carbon nanotubes as quantum wires. *Nature* 386: 474–477.

Tans, S. J., Verschueren, A. R. M., and Dekker, C. 1998. Room-temperature transistor based on a single carbon nanotube. *Nature* 393: 49–52.

Tohji, K., Goto, T., Takahashi, H., Shinoda, Y., and Shimizu, N. 1996. Purifying single-walled nanotubes. *Nature* 383: 679.

Tsang, S. C., Chen, Y. K., Harris, P. J. F., and Green, M. L. H. 1994. A simple chemical method of opening and filling carbon nanotubes. *Nature* 372: 159–162.

Voit, J. 1994. One-dimensional Fermi liquids. *Rep. Prog. Phys*. 57: 977–1116.

Wallace, P. R. 1947. The band theory of graphite. *Phys. Rev*. 71: 622–634.

Wilder, J. W. G., Venema, L. C., Rinzler, A. G., Smalley, R. E., and Dekker, C. 1998. Electronic structure of atomically resolved carbon nanotubes. *Nature* 391: 59–52.

Yao, Z., Kane, C. L., and Dekker, C. 2000. High-field electrical transport in single-wall carbon nanotubes. *Phys. Rev. Lett*. 84: 2941–2944.

Yao, Z., Postma, H. W. Ch., Balents, L., and Dekker, C. 1999. Carbon nanotube intramolecular junctions. *Nature* 402: 273–276.